The protofilament architecture of a de novo designed coiled coil-based amyloidogenic peptide

Mônica Santos de Freitas, Raheleh Rezaei Araghi, Enrico Brandenburg, Jork Leiterer, Franziska Emmerling, Kristin Folmert, Ulla Gerling-Driessen, Benjamin Bardiaux, Christoph Böttcher, Kevin Pagel, et al.

Journal of Structural Biology 203 (2018) 263–272

Contents lists available at ScienceDirect

Journal of Structural Biology

journal homepage: www.elsevier.com/locate/yjsbi

This article is part of a Special Issue on Coiled-Coil, Fibrous & Repeat Proteins

The protofilament architecture of a *de novo* designed coiled coil-based amyloidogenic peptide☆

Mônica Santos de Freitas[a,b,c,1], Raheleh Rezaei Araghi[b], Enrico Brandenburg[b], Jork Leiterer[d], Franziska Emmerling[d], Kristin Folmert[b], Ulla I.M. Gerling-Driessen[b], Benjamin Bardiaux[e,2], Christoph Böttcher[f], Kevin Pagel[b], Anne Diehl[a], Hans v. Berlepsch[f,*], Hartmut Oschkinat[a,b,*], Beate Koksch[b,*,3]

[a] Leibniz-Institut für Molekulare Pharmakologie, Department NMR-Supported Structural Biology, Robert-Rössle-Strasse 10, 13125 Berlin, Germany
[b] Freie Universität Berlin, Department of Chemistry and Biochemistry, Takustrasse 3, 14195 Berlin, Germany
[c] Universidade Federal do Rio de Janeiro, Instituto de Bioquímica Médica Leopoldo de Meis, Centro Nacional de Biologia Estrutural e Bioimagem, Av. Carlos Chagas Filho 373, Rio de Janeiro, Brazil
[d] BAM Federal Institute for Materials Research and Testing, Richard-Willstätter-Str. 11, 12489 Berlin, Germany
[e] Institut Pasteur, Unité de Bioinformatique Structurale, CNRS UMR 3528, 75015 Paris, France
[f] Freie Universität Berlin, Research Center for Electron Microscopy, Fabeckstrasse 36a, 14195 Berlin, Germany

ARTICLE INFO

Keywords:
Amyloid fibrils
Electron microscopy

ABSTRACT

Amyloid fibrils are polymers formed by proteins under specific conditions and in many cases they are related to pathogenesis, such as Parkinson's and Alzheimer's diseases. Their hallmark is the presence of a β-sheet structure. High resolution structural data on these systems as well as information gathered from multiple complementary analytical techniques is needed, from both a fundamental and a pharmaceutical perspective. Here, a previously reported *de novo* designed, pH-switchable coiled coil-based peptide that undergoes structural transitions resulting in fibril formation under physiological conditions has been exhaustively characterized by transmission electron microscopy (TEM), cryo-TEM, atomic force microscopy (AFM), wide-angle X-ray scattering (WAXS) and solid-state NMR (ssNMR). Overall, a unique 2-dimensional carpet-like assembly composed of large coexisiting ribbon-like, tubular and funnel-like structures with a clearly resolved protofilament substructure is observed. Whereas electron microscopy and scattering data point somewhat more to a hairpin model of β-fibrils, ssNMR data obtained from samples with selectively labelled peptides are in agreement with both, hairpin structures and linear arrangements.

1. Introduction

Many neurodegenerative diseases such as Alzheimer's, Parkinson's, type II diabetes, or transmissible spongiform encephalopathies are associated with the conformational transition of a folded or unfolded peptide or protein into insoluble amyloid deposits (Dobson, 2003; Selkoe, 2003). Amyloid formation, however, is not a specific feature of disease related proteins, but instead appears to be a general property of peptides and proteins (Dobson, 2002; Stefani and Dobson, 2003). Recently amyloids also gained attention in the fields of bio- and nanotechnological applications since these structures display outstanding mechanical stability and remarkably regular fibrous architectures (Cherny and Gazit, 2008; Lashuel et al., 2000; MacPhee and Woolfson, 2004). Although the precursor proteins differ widely in size and primary or secondary structure, the insoluble amyloid fibrils share a similar principal morphology (Dobson and Karplus, 1999; Makin and Serpell, 2005; Makin et al., 2005). They all appear straight and unbranched with lengths in the range of micrometers and diameters

☆ This Special Issue is edited by Andrei N. Lupas and Derek N. Woolfson, and is published as a companion to the meeting on Coiled-Coil, Fibrous & Repeat Proteins at Alpbach, Austria, September 3-8, 2017.

* Corresponding authors at: Leibniz-Institut für Molekulare Pharmakologie, Department NMR-Supported Structural Biology, Robert-Rössle-Strasse 10, 13125 Berlin, Germany (H. Oschkinat).
E-mail addresses: oschkinat@fmp-berlin.de (H. Oschkinat), beate.koksch@fu-berlin.de (B. Koksch).
[1] ORCID ID: 0000-0003-3105-7918.
[2] ORCID ID: 0000-0003-4014-9195.
[3] ORCID ID: 0000-0002-9747-0740.

https://doi.org/10.1016/j.jsb.2018.05.009
Received 14 January 2018; Received in revised form 25 May 2018; Accepted 28 May 2018
Available online 29 May 2018

typically up to ~250 Å. Circular dichroism (CD) spectroscopy reveals a high β-sheet content of the fibrils. X-ray fiber diffraction shows a characteristic anisotropic cross-β diffraction pattern in which β-strands run perpendicular to the fiber axis (Eanes and Glenner, 1968; Kirschner et al., 1986; Makin and Serpell, 2005; Sunde et al., 1997). Morphological studies using transmission electron microscopy (TEM) or atomic force microscopy (AFM) show that amyloid fibrils commonly consist of a small number of protofilaments with typical diameters in the range of 20–160 Å (Chamberlain et al., 2000; Makin and Serpell, 2005).

The process of amyloid formation has been intensively studied over many years, but the underlying molecular mechanisms remain difficult to elucidate and are likely not generalizable across sequences. Due to the low solubility of amyloid forming proteins and their intrinsically high tendency to aggregate, the use of techniques such as solution-based NMR or X-ray crystallography (Apostol et al., 2010; Nelson et al., 2005) is limited and this often precludes detailed characterization at atomic resolution. Furthermore, amyloid structures sometimes display high degrees of heterogeneity (Psonka-Antonczyk et al., 2016) and polymorphism, and it has been shown that in such cases much information can be obtained by applying multiple distinct analytical techniques (Fitzpatrick et al., 2013). For example, systematic (e.g., alanine) scanning approaches combined with low resolution techniques have been used to assign functions to specific residues (Williams et al., 2006) or secondary structure elements (Gerling et al., 2011; Morimoto et al., 2004; Williams et al., 2004) within the sequences of amyloidogenic peptides. However, gaining information about the molecular details of amyloid structures requires high resolution techniques. One increasingly common method is ssNMR analysis, which uses suitably isotope labelled samples for obtaining sequence-specific resonance assignments (Hong, 1999a; Pauli et al., 2001; Straus et al., 1998) and to estimate distance restraints and torsion angles (Brown and Spiess, 2001; Hong, 1999b; Jaroniec et al., 2001). By means of this technique, several structures of many disease-related peptides and proteins in their fibrillar form have been resolved over the years (Lührs et al., 2005; Petkova et al., 2004; Petkova et al., 2002; Tycko, 2011). Progress in sample preparation and ssNMR itself, and especially in combination with EM and even IR techniques, have enabled important recent determinations of high resolution fibril structures (Eisenberg and Sawaya, 2017; Gremer et al., 2017; Hoffmann et al., 2017; Qiang et al., 2017; Seo et al., 2016). These very high profile high-resolution studies, and the judicious combination of analytical techniques, have revealed novel fibril architectures that are not only staggering from a structural perspective but also provide insight into the process of fibril growth and morphological characteristics of the end structures, which are likely to be distinct for each amyloid forming sequence and heavily dependent upon the environment it is in. In previous work our group established a series of *de novo* designed coiled coil-based model peptides that are able to undergo structural transitions to β-sheet rich amyloid fibrils, and their conformation can be switched in response to shifts in pH, ionic strength, or metal ion concentration (Brandenburg et al., 2012; Brandenburg et al., 2011; Gerling et al., 2014; Pagel and Koksch, 2008; Pagel et al., 2005; Pagel et al., 2006; Pagel et al., 2008a; Pagel et al., 2008b).

In the present study we have used a combination of TEM, AFM, WAXS, and ssNMR to characterize the amyloid structure of the previously designed model peptide RR01 (Pagel et al., 2008a). RR01 exhibits glutamate based pH-switchable folding behavior. Under acidic conditions, the peptide forms α-helical fibers, whereas a concentration-dependent, conformational transition from a random coil structure toward amyloid fibrils occurs at neutral pH. Electron microscopic investigations reveal distinct polymorphic structures like funnels, tubes and ribbons. However, the protofilament substructure is clearly visible and highly regular for all individual fibril morphologies. Additional AFM and WAXS were performed to provide further quantitative structural data on the nanometer scale. Molecular information was gained from high resolution, solid state NMR experiments of several RR01 variants containing ^{15}N – and ^{13}C-labeled amino acids at strategic positions in the sequence. Based on our results, a structural model for the molecular arrangement of peptide strands within the fibril was deduced.

2. Materials and methods

2.1. Peptide synthesis and purification

Peptides were synthesized on a Multi-Syntech Syro XP peptide synthesizer at solid-phase using the Fmoc strategy and Fmoc-Leu-OWang resin (0.65 mmol/g). The ^{13}C or ^{15}N-labeled amino acids were manually introduced using HOBt/DIC activation and elongated coupling times. For UV concentration determination, the peptides were N-terminally labeled with anthranilic acid (Abz). Peptides were cleaved from the resin by reaction with 4 mL of a solution containing 10% (w/v) TIPS, 1% (w/v) water, and 89% (w/v) TFA. The crude peptides were purified by reversed-phase HPLC on a Knauer smartline manager 5000 system, equipped with a C8 (10 μm) LUNA™ phenomenex column. The peptides were eluted with a linear gradient of ACN/water/0.1% TFA and identified by MALDI-ToF MS using a Bruker Reflex III spectrometer with a ToF mass analyzer. Peptide purity was determined by analytical HPLC on a Merck LaChrom system equipped with a C8 (10 μm) LUNA™ phenomenex column. The used gradients were similar to those of the preparative HPLC.

2.2. Fibril formation

Lyophylized peptide was dissolved in HFIP and sonicated for 15 min at room temperature. A certain amount of the stock solution was taken and the HFIP was removed under a gentle stream of argon. The resulting film was dissolved in 1 mL 10 mM phosphate buffer (pH 7.4) and the concentration was determined by UV spectroscopy at 320 nm using a Varian Cary 50 spectrophotometer (Varian Medical Systems, Palo Alto, CA, USA) and PMMA cuvettes (10 mm path length, 1.5 mL, Plastibrand®, VWR International GmbH, Darmstadt, Germany). Prior to analysis a calibration curve with Abz-Gly-OH (Bachem GmbH, Weil am Rhein, Germany) in phosphate buffer (10 mM, pH 7.4) was recorded at different concentrations. Samples were stored at −20 °C until they were used. Peptides were dissolved in freshly prepared buffer according to the conditions required for the particular analysis. Fibrils were formed by incubation at 25 °C under stationary conditions.

2.3. WAXS

2.3.1. Sample preparation

Amyloid fibrils were formed by dissolution of the purified peptide in freshly filtered 10 mM Tris-HCl buffer (pH 7.4), followed by incubation for 7–10 days at room temperature. Some of the WAXS samples at pH 7.4 were prepared in Millipore water instead of buffer, whereas the pH was adjusted by adding small amounts of HCl or NaOH, respectively. Thus, these samples contained only NaCl crystals after drying, which simplified the assignment of X-ray reflections. β-Sheet content was determined by CD spectroscopy and amyloid formation with direct visualization by TEM. Peptide concentration was calculated based on the absorption at 320 nm. The final concentrations were in the 200–1000 μM range. The intensity of the observed WAXS reflections, relative to the solvent background scattering, increases with the packing density of the fibrils. Therefore a high concentration of peptide is desirable that is commonly achieved by drying the peptide suspension (Stubbs, 1999). We have attempted several methods of specimen preparation. The most simple procedure, which produces a thin film, is to dry an aliquot of the original peptide solution (1 mM) within an Eppendorf tube. To prepare oriented specimens a droplet of concentrated fibril solution was dried between the siliconized ends of two glass capillaries which were held ~1.5 mm apart (Morris and Serpell,

2010). The hydrated pellets were produced using two different routes. In the first case, the concentration of the sample was accomplished by centrifugation at 60,000 rpm (~150,000*g*) for two hours at 8 °C in a Beckman Optima™ TLX ultracentrifuge and discarding the supernatant followed thereafter. In the second case, the original peptide solution was concentrated by evaporation of water under reduced pressure. The peptide concentration in both pellets was in the order of 10 mM. An effect of the preparation route on the WAXS results has not been observed.

2.3.2. X-ray diffraction

All X-ray scattering experiments were performed using the micro focus beamline (μSpot) at BESSY in Berlin. Details on the beam line setups were reported previously (Paris et al., 2007). Dried specimens obtained by air drying in Eppendorf tubes were fixed on a thin polyester tape (scotch tape, Carl Roth GmbH, Karlsruhe, Germany). Alternatively an ultrasonic levitator (Tec5, Oberursel, Germany) was integrated in the setup at the synchrotron to allow containerless measurements of liquid samples in air (Leiterer et al., 2008). One ~5 μL droplet of the concentrated amyloid solution (soft pellet) was directly hand-injected by an Eppendorf pipette. A microscope with an optical camera provided information on the exact position, shape, and size of the levitated sample. For the X-ray scattering measurements a beam of about 300 μm at the focus position was used. The beam divergence was less than 1 mrad (horizontally and vertically) at a photon flux of $1 \times 10^9\,s^{-1}$ and a ring current of 100 mA. All experiments were carried out with highly monochromatic X-rays from a double crystal monochromator and, alternatively, a multi-layer monochromator ($9\,keV < E < 15\,keV$, bandwidth $10^{-4} < \Delta E/E < 10^{-2}$). The scattered intensity at a wavelength of $\lambda = 1.0024$ Å was collected by a 2D MarMosaic CCD detector (3072 × 3072 pixel at a point spread function width of about 100 μm). The sample-to detector distance was varied between 200 and 300 mm. The exposure time ranged from 10 s to 10 min depending on the scattering contrast of the samples. Corundum powder with a mean grain size smaller than 10 μm (Sigma-Aldrich) was used to calibrate the measuring setup. 1D scattering profiles were obtained by azimuthally averaging the 2D patterns using the program FIT2D (Hammersley, 1998). Isotropic 2D patterns were integrated over the whole angle range of 360°, whereas a sector-averaging was carried out when anisotropic patterns were used. After the averaging the 1D scattering profiles of dried samples were corrected for the background. Here the scattering of the supporting polyester tape (scotch tape) was subtracted, or, in the absence of a support, the scattering of an empty sample (air scattering) was used. For 1D scattering profiles of pellets obtained by the measurement with the levitator, a background was not subtracted, but all curves were normalized to an identical intensity at a scattering vector of $q = 4\,Å^{-1}$.

2.3.3. Electron microscopy

For staining electron microscopy aliquots of 7 μL of peptide solutions were absorbed for 1 min to glow-discharged carbon-coated collodium films on 400-mesh copper grids. After blotting and staining with 1% phosphotungstic acid (PTA) the grids were air-dried. TEM micrographs were taken at a primary magnification of 58,300 using a defocus of 0.7 μm. Electron micrographs revealing the surface topography of fibrils were taken from samples deposited on carbon films, air-dried and subsequently Pt/C shadowed at an inclination angle of 35°. TEM micrographs were taken at a primary magnification of 16,700 using a defocus of 2.0 μm. The samples for cryo-TEM were prepared at room temperature by placing a droplet (7 μL) of the peptide solution on a hydrophilized perforated carbon filmed grid (60 s Plasma treatment at 8 W using a BALTEC MED 020 device). The excess fluid was blotted off to create an ultrathin layer of the solution spanning the holes of the carbon film. The grids were immediately vitrified in liquid ethane at its freezing point (−184 °C) using a standard plunging device. The vitrified samples were transferred under liquid nitrogen into a Philips CM12 transmission electron microscope using the Gatan cryoholder and -stage (Model 626). Microscopy was carried out at −175 °C sample temperature using the microscope's low dose protocol at a primary magnification of 58,300. A defocus of 1.5 μm was chosen.

2.3.4. Atomic force microscopy

Measurements were performed using a standard nanoscope (Multimode IIIa, Digital Instruments, Santa Barbara, CA, USA). The microscope was operated in the tapping mode, using silicone probes at resonance frequencies of 330 kHz under ambient conditions. The cantilever was forced to oscillate near its resonance frequency. The force constant of the 125 μm long silicon cantilevers (SSS-NCH) used was 42 N/m with probes of a curvature radius better 20 Å (nanosensors, Jena, Germany). The image data have been subjected to a first-order flattening. Prior to analysis by AFM, the fibrils were diluted 1/10 in Millipore water. The samples were prepared by spin-coating. Spin-coating was carried out by depositing a 20 μL droplet of the solution on a freshly cleaved mica surface that was spun at 2000 rpm for 2 min.

2.3.5. Solid-state NMR

The experiments were performed on a wide bore NMR spectrometer with a static magnetic field of 14 T (Bruker, Avance III) using 3.2 or 4 mm triple resonance ($^1H/^{13}C/^{15}N$) probes. For all experiments, the nominal temperature was 2 °C. Spinal64 φ15° proton decoupling was applied during the first evolution period and the acquisition time, with the r.f. amplitude set to 85 kHz.

NCA and NCO spectra were recorded with specific-CP (Baldus et al., 1998), whereby the CA offset was adjusted to 6790.6 Hz and the CO offset to 24210.2 Hz. The Hartmann-Hahn condition was matched with $\omega_{1C}/2\pi$ of 25 kHz and $\omega_{1N}/2\pi$ of 35 kHz, applying a "TangAmpMod" shaped pulse on CA or CO with Delta MAS set to 5000 Hz, dipolar coupling set to 500 Hz and the RF field at match to 25,000 Hz with the Amplitude Scaling Factor to 50%. The spectrum was recorded with acquisition times of 6.5 ms (32 points) and 12 ms (1194 points) in t_1 and t_2, respectively. The recycle delay was 2.8 s and 960 and 736 scans were acquired for NCA and NCO, respectively. A 2D TEDOR (Hing et al., 1992) spectrum with a mixing time of 5 ms was recorded. The ^{15}N REDOR π pulse length was 10 μs, the ^{15}N and ^{13}C π/2 pulses were 5 μs and 3.5 μs, respectively. The spectrum was recorded with acquisition times in t_1 and t_2 of 4 ms (32 points) and 12 ms (1706 points), respectively. The recycle delay was set to 2.7 s, and 1664 scans were acquired.

^{13}C-^{13}C correlation spectra were recorded with PDSD (Szeverenyi et al., 1982) mixing, applying mixing times of 25 and 500 ms, and values in between. The spectra were typically recorded with t_1 and t_2 times of 4.2 ms (320 points) and 12 ms (1194 points), respectively. Recycle delays were approximately 3 s, and the number of scans was dependent upon the signal to noise, with the range being from 80 to 448. The acquired data were processed in Topspin 3.2 (Bruker) with Lorentz-to-Gauss transformation and squared sine bell 3 apodization as window functions in the direct and indirect dimension, respectively. We further applied linear prediction and two- and fourfold zero filling in the indirect and direct dimensions, respectively. The data were analyzed using CcpNMR (Stevens et al., 2011; Vranken et al., 2005).

2.4. Molecular models and theoretical density profiles for RR01 fibers

For each arrangement of peptide strands, 1000 conformers were calculated by simulated annealing using ARIA (Rieping et al., 2007). The inputs were ssNMR distance restraints (V_3-K_{23}, E_{10}-K_{16}, E_{10}-S_{17}), backbone dihedral angle restraints predicted from chemical shifts using TALOS+ (Shen et al., 2009), C2 symmetry restraints between monomers and hydrogen bond restraints between copies of a single dimer along the fiber axis (4.7 Å translation in both directions of the axis). For the hairpin arrangement, V_3-K_{23} was considered as intra and inter monomeric restraint and E_{10}-K_{16}, E_{10}-S_{17} as intra-monomeric restraints.

Table 1
Isotopic labeling patterns of RR01 fibril samples for NMR.

Sample Name	Amino Acid Sequence and Labeled Positions
RR01	Abz-LKVELKELKEELVVLKSELKELKEEL-OH
u-$^{13}C^{15}N$-$V_3V_{14}L_{15}$	Abz-LKVELKELKEELVVLKSELKELKEEL-OH
u-$^{13}C^{15}N$-$L_1V_3L_{19}K_{23}$	Abz-LKVELKELKEELVVLKSELKELKEEL-OH
u-$^{13}C^{15}N$-$V_3L_5L_{12}V_{13}$	Abz-LKVELKELKEELVVLKSELKELKEEL-OH
u-$^{13}C^{15}N$-$V_3L_5E_{10}K_{16}S_{17}L_{22}$	Abz-LKVELKELKEELVVLKSELKELKEEL-OH
80% - unlabeled 20% - u-$^{13}C^{15}N$-$V_3L_5E_{10}K_{16}S_{17}L_{22}$	Abz-LKVELKELKEELVVLKSELKELKEEL-OH Abz-LKVELKELKEELVVLKSELKELKEEL-OH
2-$^{13}C^{15}N$	LKVELKELKEELVVLKSELKE**L**KEEL
20% back-protonated -$^{2}H^{13}C^{15}N$	LKVELKELKEELVVLKSELKE**L**KEEL
Labeled residues are in green. "u" represents "uniformly labeled". 2-$^{13}C^{15}N$ indicates a [2-^{13}C] glycerol labeling pattern.	

For the linear arrangement, V_3-K_{23}, E_{10}-K_{16} and E_{10}-S_{17} were considered as inter-monomeric restraints. Tetrameric models were constructed by placing two dimers as close as possible without generating steric clashes along the β-strand axis. Theoretical density profiles for doublets of the two proposed models were calculated by projecting the atomic coordinates on a 2D grid parallel to the plane formed by β-sheets (averaged over the 100 lowest-energy conformers and weighted according to the RMSF in the ensemble to reflect the lower density in highly flexible regions). Finally, the density profile is computed as the average of the density grid along the fiber axis.

3. Results and discussion

3.1. Peptide design and synthesis

As mentioned briefly in the introduction, the RR01 peptide was designed and initially characterized in prior work, in which it was referred to as Peptide B, and the sequence is given and depicted in helical wheel fashion in Table 1 and Fig. 1, respectively (Pagel et al., 2008a). The design elements include i) three valine residues that make the system prone to amyloid formation but do not preclude coiled-coil assembly, ii) a pattern of glutamate and lysine residues at positions *e* and *g* that enable favorable interhelical electrostatic interactions and stabilize α-helical coiled-coil folding under acidic conditions; the glutamates can be thought of as forming an extended domain along one side of the helical cylinder that is negatively charged at neutral pH values and results in intramolecular Coulomb repulsions that destabilize the α-helical coiled coil arrangement and favor the competing amyloid form under such conditions. Circular dichroism (CD) spectroscopy revealed that when the pH switch is in the "off" state (pH 4.0) RR01 assembles into α-helical coiled-coils, but when the pH switch is in the "on" position (pH 7.4) a transition from random coil to β-sheet leading to fibril formation is observed. In order to obtain detailed information about fibril architecture the RR01 peptide and several appropriately isotopically labeled variants were synthesized (Table 1).

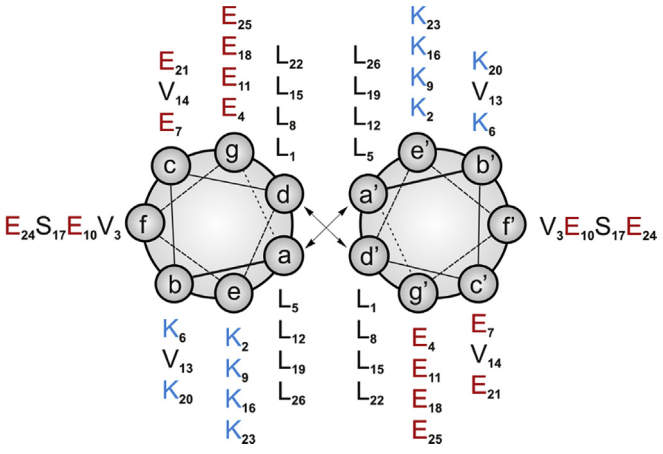

Fig. 1. Helical wheel representation of RR01.

3.2. Overview of applied analytical techniques

Amyloids formed by peptides and proteins are not able to be crystallized, with the exception of oligomeric peptides. Due to this lack of long-range order X-ray crystallography, the standard method for structural characterization, is unsuccessful. In spite of this, numerous alternative methods exist that enable structure elucidation. Best established among these are microscopic imaging techniques for determining morphology and solid state NMR (ssNMR) spectroscopy, which yields molecular structural restraints. We have applied the standard methods cryo-TEM and negative staining TEM to study the morphology of the amyloid fibrils reported here. Both approaches provide density profiles, in particular quantitative data on the dimensions and organization of the protofilaments, in the natural environment of the solvent and subsequent to deposition on a support, respectively. Theoretical simulation of the experimentally obtained density profiles can be carried out and this enables alternative molecular packing models to be evaluated. Topographic techniques such as TEM after tilt shadowing and AFM provide additional data on the three-dimensional structure of the fibrils (degree of twist and handedness). Furthermore, AFM makes possible the precise determination of thickness of the fibrils, if these were able to be successfully deposited on the surface. X-ray diffraction from a synchrotron source was used, in the large angle regime, to gain information about the core structure, in particular the stacking and orientation of the β-sheets, and, in the small angle regime, to obtain additional data on the superstructure of the fibrils, especially the protofilaments. All of these methods yielded consistent results that enabled a quantitative description of fibril morphology. The goal of the ssNMR experiments was to develop a molecular model for the fibril architecture from structural restraints. For this purpose, short distances were measured between individually labelled amino acids, and chemical shifts interpreted with regard to the indicated secondary structure. This yielded two models for the fine structure of the monomers, which may both be present in a fibril according to two different forms observed in ^{13}C-^{13}C correlations, one shows extended protomers, the other is proposed to adopt a loop

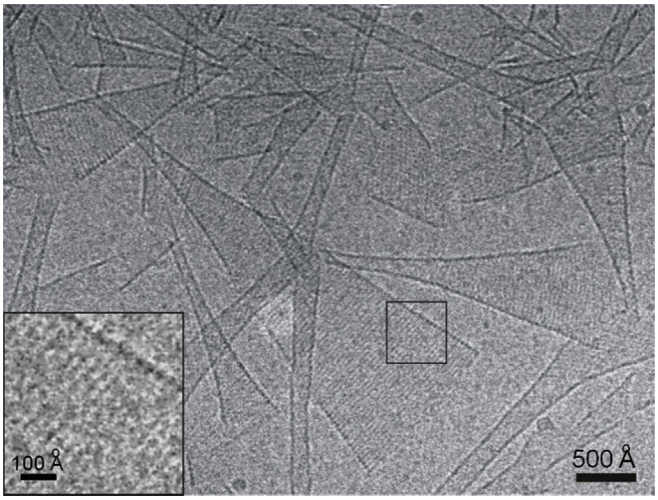

Fig. 2. Cryo-TEM micrograph of a 375 μM peptide sample of RR01 showing amyloid structures at pH 7.4 after 10 days of incubation. Flat, twisted, and tubular morphologies coexist. The inset shows the boxed region at high magnification. The protofilaments are well resolved.

conformation involving V14 and L15. Extended and hairpin-like structures can potentially assemble to a fibril that satisfies the EM constraints.

3.3. Fibril morphology by TEM

Fig. 2 shows a representative cryo-TEM micrograph of the amyloid structures of RR01 after incubation for 10 days at pH 7.4. A mixture of tubular structures, sometimes showing funnel-like ends, are frequently found in addition to twisted ribbons. Noticeable is the enormous width of the structures, which can reach values on the order of 1000 Å. A typical TEM micrograph after negative staining of a narrow ribbon is depicted in Fig. 3. A line scan across the ribbon axis reveals that it is composed of two laterally associated strands of ~70 Å width. The cross-sectional density profile of the fibril is characterized by two regions of high density at the ends and one of less density in the middle, which indicates that the elementary strand consists of two ~35 Å wide protofilaments. Another example of a narrow ribbon composed of four strands (8 protofilaments) is shown in Fig. S1. Such narrow ribbons are rare. These were found to disappear within several weeks of incubation and to be replaced by helical tubes (Fig. S2). All cryo-TEM micrographs of the several polymorphic amyloid structures show the highly regular line pattern with the typical distance of ~35 Å. Averaging and profiling (Fig. S2) reveals that the lines are arranged pairwise, i.e. the repetition period of the ultrastructure is twice that distance (2 × 35 Å = 70 Å). TEM after metal shadowing provides surface reliefs of the ribbon-like and tubular amyloids (Fig. S3) again with a repetition period of ~70 Å, confirming the ultrastructure visualized by the cryo preparation.

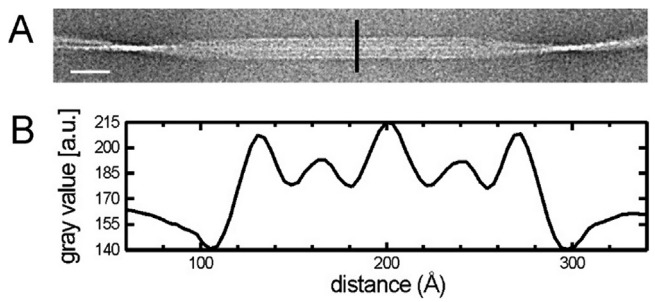

Fig. 3. TEM micrograph of a doublet fibril and corresponding density profile for RR01. *(A)* TEM image after PTA staining. Scale bar (left): 300 Å. *(B)* Line scan along the dark line in panel *A*.

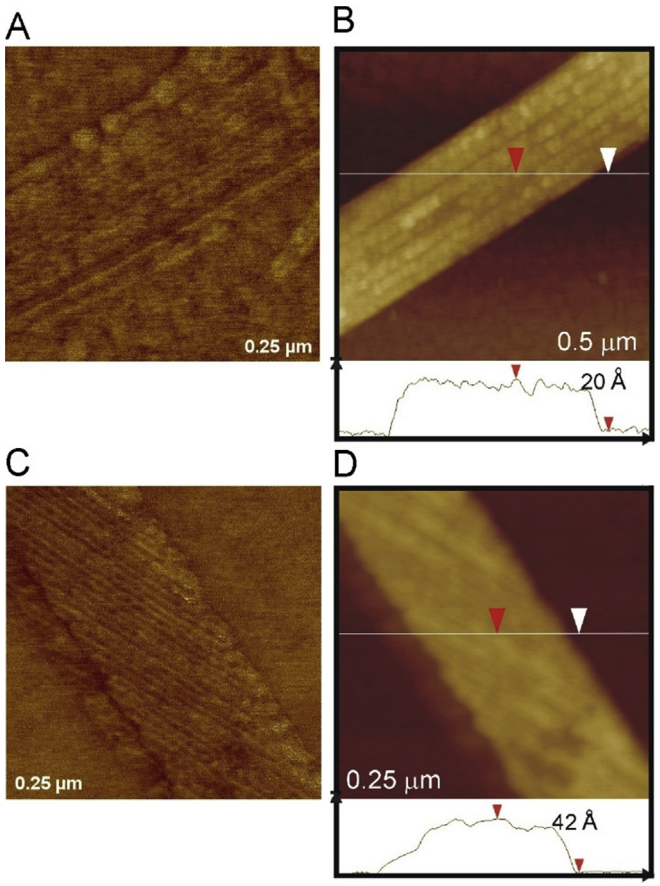

Fig. 4. AFM images of ribbon-like and tubular amyloids of RR01. *(A)* Phase image (0.25 μm × 0.25 μm) of a ribbon-like fibril. The lateral stripes reveal a hierarchical buildup of interconnected 70.0 ± 5 Å wide elementary fibrils. *(B)* Topography image (0.5 μm × 0.5 μm) of a ribbon-like fibril and height profile along the line indicated. *(C)* Phase image (0.25 μm × 0.25 μm) of a tubular fibril. The inclined stripes reveal the helical buildup of 66.5 ± 4 Å wide elementary fibrils. *(D)* Topography image (0.25 μm × 0.25 μm) of a tubular fibril and height profile along the line indicated. The height of the collapsed tube is about twice that of the ribbon shown in panel *B*.

To obtain quantitative information on the thickness of the fibrils, AFM has been employed. An overview image (Fig. S4) shows ribbon-like and tubular aggregates. Both types can easily be discriminated by their characteristic stripe patterns and differing heights. AFM topography images of a ribbon and a tube at higher resolution are presented in Fig. 4B and D together with height profiles along the indicated lines, showing a thickness of approximately 20 Å. This value roughly agrees with the estimate of ribbons thickness obtained from negative stain TEM micrographs (Fig. S1). One would expect the tube to be collapsed to form a more or less flat layer as well. Indeed, the obtained height profile is rather plain and the maximum height corresponds to approximately twice that of the single ribbon. Corresponding high-resolution AFM phase images are shown in Fig. 4A and C. The typical stripe pattern due to the fibrillar ultrastructure is well discernable here. The Fourier transform from the images gives repetition periods of 70 and 66.5 Å for the ribbons and tubes, respectively. These are just the same values as for the metal shadowed EM specimen.

3.4. X-ray characterization

Dried samples of RR01 fibrils were subjected to WAXS and gave the scattering profile shown in Fig. 5. The three reflections with *d*-spacings at 3.8, 4.7, and ~10 Å (diffuse), respectively, are typical for many peptides forming β-sheets (Makin and Serpell, 2005). The sharp

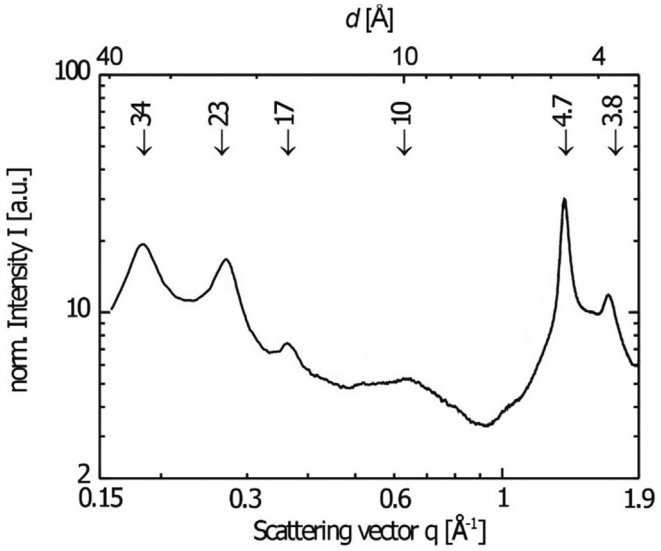

Fig. 5. Scattering profile obtained from a dried fibril sample of RR01. The correlating *d*-spacings of prominent reflections are indicated by arrows.

reflection at 4.69 Å corresponds to the distance between the β-strands comprising the β-sheets and the diffuse reflection at 10 Å is commonly ascribed to the distance between the β-sheets (Geddes et al., 1968). The reflection at around 3.8 Å is frequently observed for amyloids. It has been previously indexed as the (2 1 0) reflection for the orthogonal unit cell formed by the amyloid β-crystallites (Fraser et al., 1992; Kirschner et al., 1987). Additional WAXS reflections at large *d*-spacings, i.e., at around 17, 23, and 34 Å are found. The prominent 34 Å reflection is in good agreement with the lateral repetition period of the protofilaments. These findings suggest that the scattering reflections in the low-*q* region are related to protofilament ordering.

In situ dehydration experiments (Fraser et al., 1991; Squires et al., 2006) were conducted using the levitation method (Leiterer et al., 2008). A pellet of the peptide fibril suspension was placed in the X-ray beam, while a complete 2D scattering pattern was recorded every 20 s. Typical for all scattering profiles (Fig. S5) is the sharp reflection corresponding to $d \sim 4.7$ Å and the broad maximum corresponding to $d \sim 10$ Å. Both are β-sheet related reflections which have already been found for the dried samples. Their obvious independence on the evaporation time once more confirms that the distance between the peptide strands forming the β-sheets and their stacking distance remained unaffected by the level of hydration. The reflections at $q < 0.5$ Å^{-1} ($d > 12$ Å) show a strong dependence on the level of hydration (Fig. S6). For the starting solution only one weak and diffuse reflection was found at around 23.6 Å, which turned into a well resolved peak upon progressive dehydration. In addition, two further reflections corresponding to spacings of 34.0 and 17.3 Å evolved. The maximum positions of all three reflections remained fixed for the entire observation period. The nearly perfect coincidence of the 34 Å reflection with the inter-protofilament spacing of ~35 Å measured by cryo-TEM is noticeable. The additional reflection at 17.3 Å is likely to be the harmonic of the 34 Å reflection (the ratio of *d*-spacings is 1/2). The very stable reflection corresponding to a *d*-value of 23.6 Å has no counterpart in the cryo-TEM micrographs, but might be connected with the spacing of vertically stacked aggregates whose thickness was estimated by AFM and negative staining TEM to be on the order of 20 Å.

The morphological investigations revealed two well-defined mesoscopic polymorphs, namely ribbons and tubes in different proportions. The most frequent form identified by TEM and AFM was the ribbon structure. However, quantitative image analysis supported by WAXS revealed a universal ultrastructure, suggesting that the various polymorphic structures are all composed of laterally assembled elementary fibrils, whose number differs in general, and which themselves consist of two ~35 Å wide protofilaments. Solid-state NMR analysis should help to understand the molecular structure of these elementary fibrils and their preferred lateral assembly.

3.5. Structural models from distance restraints

Based on the cryo-TEM, TEM and WAXS results, the RR01 fibrils are composed of two well-defined forms, ribbons and tubes that are in different proportions. The form most frequently found by TEM is the ribbon structure, which we henceforth consider to be the major form. In order to obtain sequential resonance assignments for RR01 fibrils at pH 7.4, several samples with individual residues in ^{13}C, ^{15}N-labeled form were prepared as indicated above in Table 1 (see also therein defined sample notation). 2D ^{13}C, ^{13}C spin diffusion experiments with short (20 ms) and long (500 ms) mixing times were carried out on u-^{13}C^{15}N-$V_3V_{14}L_{15}$ (Fig. S8A), u-^{13}C^{15}N-$L_1V_3L_{19}K_{23}$ (Fig. S9A) and u-^{13}C^{15}N-$V_3L_5L_{12}V_{13}$ (Fig. S8B) fibrils. The small ^{13}Cα, ^{13}Cβ and ^{13}CO chemical shift differences between V_3 and V_{14} required an NC correlation experiment to properly assign those residues. Surprisingly, five signals corresponding to the labelled residues were observed in the 2D NCA spectrum of u-^{13}C^{15}N-$V_3V_{14}L_{15}$, whereas only three peaks had been expected (Fig. S8A). Similarly, the 2D ^{13}C, ^{13}C spin diffusion experiment showed clearly the pattern of one additional leucine and valine signal set, albeit at lower intensity. This result suggests the presence of two different conformations, respectively chemical environments, for V_{14} and L_{15} (Fig. S8A).

Secondary structure was probed by comparing the ^{13}CO, ^{13}Cα and ^{13}Cβ chemical shifts in relation to random coil values (Table S1). In general, the shifts of the ^{13}C^{15}N-labeled residues displayed chemical shift values correlating with a β-strand environment than a helical conformation, in agreement with the WAXS analysis (Fig. 5). Similarly, the NH-correlation showed solely β-sheet content, with the lowest amide proton chemical shift above 8.8 ppm. However, the ^{13}Cα and ^{13}Cβ chemical shifts of the second signal sets observed for V14 and L15 indicate a loop-like or helical environment for the respective residues in the minor conformation. The presence of very strong intraresidual cross-peaks for ^{13}C^{15}N-labeled amino acids from V_3 to K_{23} in the various spectra indicates that the entirety of the fibril is rigid. A 1D ^{13}C spectrum with INEPT transfer (Morris and Freeman, 1979) on fully protonated RR01 fibrils was acquired and no signal appeared, which again indicates the absence of mobile regions. Moreover, for 20% back protonated 2-^{13}C^{15}N RR01 fibrils, 2D ^{1}H^{15}N-INEPT- and ^{1}H^{15}N-CP-based spectra (Figs. S10A and S10B, respectively) are very similar, without any signals around 8.3 ppm in F_2 occurring in the INEPT spectrum, which again indicates the rigidity of RR01 fibrils over the entire amino acid sequence.

The chemical shift assignments obtained for RR01 fibrils were used to model a structure of the fibril core. Long-range connectivities between V_3 and K_{23} were clearly observed in the spectra of the sample containing ^{13}C^{15}N-$L_1V_3L_{19}K_{23}$ fibrils at a spin-diffusion mixing time of 500 ms (Fig. S9A). This indicates spatial proximity of the two ends of RR01, yet it is unclear whether it represents intra or inter-strand correlation. Additional long-range and unambiguous distance restraints were determined from a spin-diffusion experiment of 500 ms on ^{13}C^{15}N-$V_3L_5E_{10}K_{16}S_{17}L_{22}$ RR01 fibrils (Fig. S9B). The cross-peaks between E_{10}-K_{16} and E_{10}-S_{17} support the connection of residues placed in the middle of RR01 units that, in combination with the distance restraint found for V_3-K_{23}, are in agreement with two structural possibilities for the fibril backbone: a hairpin or a linear arrangement. To determine the nature of the E_{10}-K_{16} and E_{10}-S_{17} interactions in terms of intra or intermolecular connectivities, diluted fibrils were prepared in the presence of 20% ^{13}C^{15}N-$V_3L_5E_{10}K_{16}S_{17}L_{22}$ and 80% unlabeled RR01 peptide (Fig. S9B). Cross-peaks due to intermolecular contacts between E_{10} and S_{17} are then expected to be weaker in comparison to cross peaks between signals of nuclei within the labelled amino acids since most labelled molecules are surrounded by unlabeled ones. In the case of

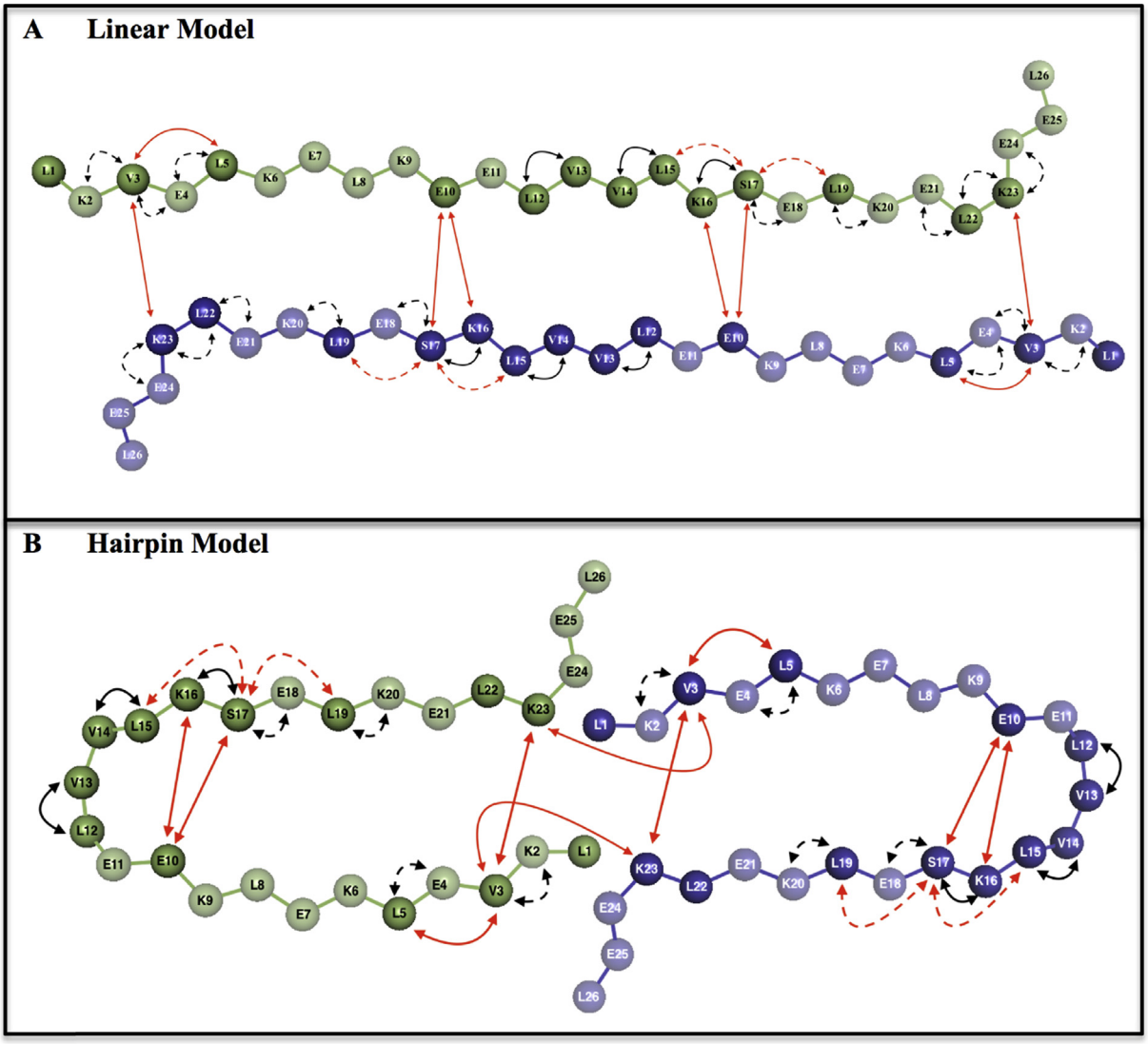

Fig. 6. Cartoon representation of short distances obtained by ssNMR of RR01 fibrils at pH 7.4. (A) The linear model is represented as extended β-strands arranged in a head-to-tail fashion. (B) The hairpin model is illustrated as a dimer of U-shaped strand-turn-strand peptides. In both cases, the green and blue colors indicate two different monomers that contain unlabeled (opaque) and $^{13}C^{15}N$-labeled (solid) amino acids. Black dashed or solid arrows indicate sequential non-ambiguous or ambiguous constraints, respectively. Red dashed or solid arrows indicate long-range ambiguous or non-ambiguous constraints, respectively.

intramolecular cross-peaks involving the two residues the relative intensity of the signals might remain unchanged. The ^{13}C-^{13}C spin diffusion experiment with a mixing time of 500 ms recorded on a diluted sample did not show a conclusive result with regard to the correlations E_{10}-K_{16} and E_{10}-S_{17}. The crucial signals at 63.5 ppm in F_1 (S_{17} Cβ) and around 35 ppm in F_2 (E_{10} Cβ and Cγ) visible in the black spectrum of Fig. S9B are absent from the spectrum of the mixed sample (red spectrum, see black circle in Fig. S9B). However, a cross peak appeared close by in the spectrum of the mixed sample, that might be due to the interaction S_{17} – $E_{10,}$ although it is more likely that now a correlation involving the signals of S_{17} Cβ and K_{16} Cβ occurs, given the slightly different chemical shift in F_2. Due to these doubts, those crucial signals were not safely assignable as intra-molecular or as originating from two different strands, hence they were treated as ambiguous. In a similar manner, the cross-peaks between V_3-L_{22} and V_3-L_5 were assigned as ambiguous. The summary of all distance restraints detected for RR01 fibrils are illustrated in Fig. 6, showing the long range restraints in a linear model (Fig. 6A) and in a hairpin model (Fig. 6B).

In an attempt to distinguish between the two possibilities, structure calculations were carried out whereby distance restraints between V_3-K_{23} and E_{10}-K_{16} and E_{10}-S_{17} were considered either intra- or intermonomer. Views of the calculated RR01 fibril models with the lowest energy illustrate the packing for hairpin or linear arrangements (Fig. 7A). To compare the molecular models calculated from ssNMR data with EM analysis, theoretical density profiles of the generated models were computed (Fig. S11). The theoretical density profile of the hairpin arrangement is better correlated to TEM analysis of doublet fibrils than the linear model (Fig. 7B).

4. Conclusion

Determining how the amino acid sequence of a protein relates to the higher order structures it adopts, and how this in turn enables its function, or its pathogenicity, remains one of the greatest challenges in biomedical science. A task that is already extraordinarily difficult by *ab initio* means without using templates (Dill and MacCallum, 2012; Zhang et al., 2017) is made next to impossible when one considers that the intracellular environment adds numerous parameters that dramatically impact folding. Moreover, disease-related conditions such as hyperphosphorylation or altered glycation further affect folding in ways that cannot be predicted. Here we structurally characterize fibrils formed by a peptide designed to be switchable, and, in particular, to form fibrils at

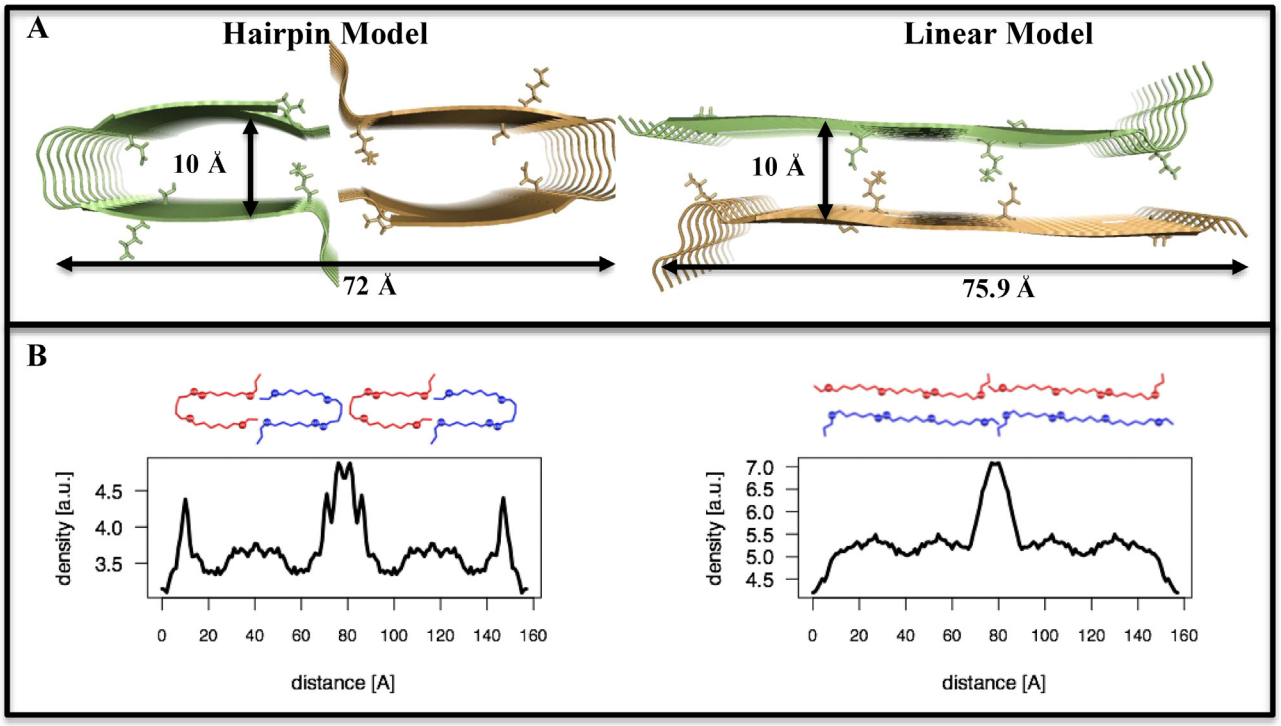

Fig. 7. Structural models for RR01 fibrils at pH 7.4. (A) Atomic view of the best energy RR01 fiber models using ssNMR restraints. The dimers formed in the hairpin model have 72 Å of extension and the linear model has 75.9 Å. (B) Average computed density profiles of RR01 fiber models.

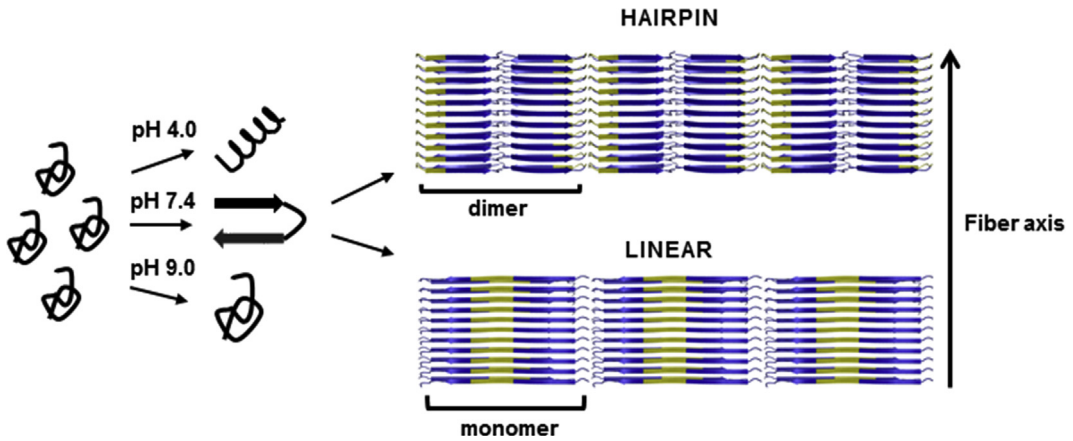

Fig. 8. Schematic diagram for RR01 peptide aggregation. At pH 4.0, an α-helical coiled coil structure is obtained and no aggregation is observed over 72 h (Pagel et al., 2008a); at pH 9.0, no defined secondary structure is observed (Pagel et al., 2008a); and at pH 7.4, the peptide adopts a β-sheet structure and polymorphic fibrils are formed. The hotspot sequence LVVLKS predicted by Aggrescan (Conchillo-Solé et al., 2007) and the TANGO (Fernandez-Escamilla et al., 2004; Linding et al., 2004; Rousseau et al., 2006) algorithm are depicted as yellow regions in the otherwise blue peptide sequence in the right panels. In the hairpin model (upper right) supported by ssNMR data, the hotspot sequence is located in the loop regions at the interfaces between dimeric β-sheet units. In contrast, the linear model (lower right) has its hotspot sequence in the central part of monomeric β-sheet units.

neutral pH.

RR01 is a pH-switchable coiled coil-based peptide that undergoes a structural transition resulting in fibril formation under physiological conditions. Its design is based on three valine residues, in *f*, *b*, and *c* positions (see Fig. 1), and a pattern of glutamate and lysine residues at positions *e* and *g* that make the system prone to the formation of α-helical coiled-coil structures under acidic conditions (pH switch "off") but lead to amyloid formation at neutral pH values (pH switch "on"). Transmission electron microscopy (TEM), cryo-TEM, atomic force microscopy (AFM), wide-angle X-ray scattering (WAXS) and ssNMR were applied to investigate the structural properties of RR01 fibrils at neutral pH. A unique 2-dimensional carpet-like assembly composed of large coexisting ribbon, tube, and funnel morphologies was observed. Most remarkable is the absence of vertical fibril growth. Whereas the microscopy and scattering data point to a hairpin model of the peptide RR01 in the β-fibrils, ssNMR data obtained from samples with selectively isotopically labelled peptides fit to two different models, a hairpin and a linear arrangement (Fig. 6). In fact, two conformations are observed, whereby the majorly populated one shows residues V_{14} and L_{15} in a strand-like environment, whereas the minor conformation suggests loop or helical structure. This observation is potentially in agreement with the presence of both, the hairpin and the linear arrangement in the produced fibrils.

Based on the data presented here, we explain the notable lack of vertical fibril propagation according to the models given in Fig. 8. In the case of the hairpin model, supported by all applied analytical

techniques, the dimer units can assemble in two dimensions: i) stacking upon one another along the fibril axis, and ii) favorably interacting with one another within the dimer plane by means of the bend regions or hydrophobic hotspots located in the center of the sequence (especially the consensus sequence covering L12, V13, V14, and L15; see Fig. S7). A third possibility, iii) would contain linear arrangements in the center of the fibril, and hairpin structures at the ends, presumably for capping, assuming that the loop-indicating Cα and Cβ chemical shifts of V_{14} and L_{15} indicate the less populated hairpins. In all cases, the reason why no fibril extension is observed in the third dimension is likely due to unfavorable intermolecular electrostatic repulsions between the glutamate rich charged domains of the peptides along their solvent-exposed faces. Thus, RR01 is a rationally designed amyloid-forming peptide, the primary structure of which encodes for a pH controlled conformational switch, that leads to a fibrillar structure propagating in only two dimensions thus forming a highly regular carpet-like superstructure distinct from other recent detailed structural studies of fibrillar systems (Colvin et al., 2016; Wälti et al., 2016; Gremer et al., 2017; Fitzpatrick et al., 2017). In light of numerous recent attempts to apply nature's principles to biomaterial research this unique property represents a potentially useful platform, and studies are currently underway to determine the versatility of RR01 amyloids under physiological conditions.

Acknowledgements

This work was supported by the Alexander von Humboldt Foundation Georg Forster Research Fellowship and by the CAPES-DAAD Bilateral Exchange of Academics (both awarded to M.S.F.)

Appendix A. Supplementary data

Supplementary data associated with this article can be found, in the online version, at http://dx.doi.org/10.1016/j.jsb.2018.05.009.

References

Apostol, M.I., Sawaya, M.R., Cascio, D., Eisenberg, D., 2010. Crystallographic studies of prion protein (PrP) segments suggest how structural changes encoded by polymorphism at residue 129 modulate susceptibility to human prion disease. J. Biol. Chem. 285, 29671–29675.

Baldus, M., Petkova, A.T., Herzfeld, J., Griffin, R.G., 1998. Cross polarization in the tilted frame: assignment and spectral simplification in heteronuclear spin systems. Mol. Phys. 95, 1197–1207.

Brandenburg, E., Berlepsch, H.v., Koksch, B., 2012. Specific in situ discrimination of amyloid fibrils versus [small alpha]-helical fibres by the fluorophore NIAD-4. Mol. BioSystems 8, 557–564.

Brandenburg, E., von Berlepsch, H., Gerling, U.I.M., Böttcher, C., Koksch, B., 2011. Inhibition of amyloid aggregation by formation of helical assemblies. Chem. Eur. J. 17, 10651–10661.

Brown, S.P., Spiess, H.W., 2001. Advanced solid-state NMR methods for the elucidation of structure and dynamics of molecular, macromolecular, and supramolecular systems. Chem. Rev. 101, 4125–4156.

Chamberlain, A.K., MacPhee, C.E., Zurdo, J., Morozova-Roche, L.A., Hill, H.A., Dobson, C.M., Davis, J.J., 2000. Ultrastructural organization of amyloid fibrils by atomic force microscopy. Biophys. J. 79, 3282–3293.

Cherny, I., Gazit, E., 2008. Amyloids: not only pathological agents but also ordered nanomaterials. Angew. Chem. Int. Ed. Engl. 47, 4062–4069.

Colvin, M.T., Silvers, R., Ni, Q.Z., Can, T.V., Sergeyev, I., Rosay, M., Donovan, K.J., Michael, B., Wall, J., Linse, S., Griffin, R.G., 2016. Atomic resolution structure of monomorphic Aβ42 amyloid fibrils. J. Am. Chem. Soc. 138, 9663–9674.

Conchillo-Solé, O., de Groot, N.S., Avilés, F.X., Vendrell, J., Daura, X., Ventura, S., 2007. AGGRESCAN: a server for the prediction and evaluation of "hot spots" of aggregation in polypeptides. BMC Bioinformatics 8, 65.

Dill, K.A., MacCallum, J.L., 2012. The protein-folding problem, 50 years on. Science (New York, N.Y.) 338, 1042–1046.

Dobson, C.M., 2002. Getting out of shape. Nature 418, 729–730.

Dobson, C.M., 2003. Protein folding and misfolding. Nature 426, 884–890.

Dobson, C.M., Karplus, M., 1999. The fundamentals of protein folding: bringing together theory and experiment. Curr. Opin. Struct. Biol. 9, 92–101.

Eanes, E.D., Glenner, G.G., 1968. X-ray diffraction studies on amyloid filaments. J. Histochem. Cytochem. 16, 673–677.

Eisenberg, D.S., Sawaya, M.R., 2017. Structural studies of amyloid proteins at the molecular level. Annu. Rev. Biochem. 86, 69–95.

Fernandez-Escamilla, A.-M., Rousseau, F., Schymkowitz, J., Serrano, L., 2004. Prediction of sequence-dependent and mutational effects on the aggregation of peptides and proteins. Nat. Biotechnol. 22, 1302–1306.

Fitzpatrick, A.W., Debelouchina, G.T., Bayro, M.J., Clare, D.K., Caporini, M.A., Bajaj, V.S., Jaroniec, C.P., Wang, L., Ladizhansky, V., Muller, S.A., MacPhee, C.E., Waudby, C.A., Mott, H.R., De Simone, A., Knowles, T.P., Saibil, H.R., Vendruscolo, M., Orlova, E.V., Griffin, R.G., Dobson, C.M., 2013. Atomic structure and hierarchical assembly of a cross-beta amyloid fibril. PNAS 110, 5468–5473.

Fitzpatrick, A.W.P., Falcon, B., He, S., Murzin, A.G., Murshudov, G., Garringer, H.J.R., Crowther, A., Ghetti, B., Goedert, M., Scheres, S.H.W., 2017. Cryo-EM structures of tau filaments from Alzheimer's disease. Nature 547, 185–190.

Fraser, P.E., Nguyen, J.T., Surewicz, W.K., Kirschner, D.A., 1991. pH-dependent structural transitions of Alzheimer amyloid peptides. Biophys. J. 60, 1190–1201.

Fraser, P.E., Nguyen, J.T., Inouye, H., Surewicz, W.K., Selkoe, D.J., Podlisny, M.B., Kirschner, D.A., 1992. Fibril formation by primate, rodent, and Dutch-hemorrhagic analogues of Alzheimer amyloid beta-protein. Biochemistry 31, 10716–10723.

Geddes, A.J., Parker, K.D., Atkins, E.D., Beighton, E., 1968. "Cross-beta" conformation in proteins. J. Mol. Biol. 32, 343–358.

Gerling, U.I.M., Brandenburg, E., Berlepsch, H.v., Pagel, K., Koksch, B., 2011. Structure analysis of an amyloid-forming model peptide by a systematic glycine and proline scan. Biomacromolecules 12, 2988–2996.

Gerling, U.I.M., Salwiczek, M., Cadicamo, C.D., Erdbrink, H., Czekelius, C., Grage, S.L., Wadhwani, P., Ulrich, A.S., Behrends, M., Haufe, G., Koksch, B., 2014. Fluorinated amino acids in amyloid formation: a symphony of size, hydrophobicity and [small alpha]-helix propensity. Chem. Sci. 5, 819–830.

Gremer, L., Scholzel, D., Schenk, C., Reinartz, E., Labahn, J., Ravelli, R.B.G., Tusche, M., Lopez-Iglesias, C., Hoyer, W., Heise, H., Willbold, D., Schroder, G.F., 2017. Fibril structure of amyloid-beta(1–42) by cryo-electron microscopy. Science (New York, N.Y.) 358, 116–119.

Hammersley, A.P. 1998. FIT2D V9.129 Reference Manual V3.1 ESRF Internal Report.

Hing, A.W., Vega, S., Schaefer, J., 1992. Transferred-echo double-resonance NMR. J. Magn. Reson. 1969 (96), 205–209.

Hoffmann, W., Folmert, K., Moschner, J., Huang, X., von Berlepsch, H., Koksch, B., Bowers, M.T., von Helden, G., Pagel, K., 2017. NFGAIL amyloid oligomers: the onset of beta-sheet formation and the mechanism for fibril formation. J. Am. Chem. Soc.

Hong, M., 1999a. Resonance assignment of 13C/15N labeled solid proteins by two- and three-dimensional magic-angle-spinning NMR. J. Biomol. NMR 15, 1–14.

Hong, M., 1999b. Determination of multiple ***φ***-torsion angles in proteins by selective and extensive (13)C labeling and two-dimensional solid-state NMR. J. Magn. Resonance (San Diego, Calif.: 1997) 139, 389–401.

Jaroniec, C.P., Tounge, B.A., Herzfeld, J., Griffin, R.G., 2001. Frequency selective heteronuclear dipolar recoupling in rotating solids: accurate 13C–15N distance measurements in uniformly 13C,15N-labeled peptides. J. Am. Chem. Soc. 123, 3507–3519.

Kirschner, D.A., Abraham, C., Selkoe, D.J., 1986. X-ray diffraction from intraneuronal paired helical filaments and extraneuronal amyloid fibers in Alzheimer disease indicates cross-beta conformation. PNAS 83, 503–507.

Kirschner, D.A., Inouye, H., Duffy, L.K., Sinclair, A., Lind, M., Selkoe, D.J., 1987. Synthetic peptide homologous to beta protein from Alzheimer disease forms amyloid-like fibrils in vitro. PNAS 84, 6953–6957.

Lashuel, H.A., LaBrenz, S.R., Woo, L., Serpell, L.C., Kelly, J.W., 2000. Protofilaments, filaments, ribbons, and fibrils from peptidomimetic self-assembly: implications for amyloid fibril formation and materials science. J. Am. Chem. Soc. 122, 5262–5277.

Leiterer, J., Delissen, F., Emmerling, F., Thünemann, A.F., Panne, U., 2008. Structure analysis using acoustically levitated droplets. Anal. Bioanal. Chem. 391, 1221–1228.

Linding, R., Schymkowitz, J., Rousseau, F., Diella, F., Serrano, L., 2004. A comparative study of the relationship between protein structure and β-aggregation in globular and intrinsically disordered proteins. J. Mol. Biol. 342, 345–353.

Lührs, T., Ritter, C., Adrian, M., Riek-Loher, D., Bohrmann, B., Döbeli, H., Schubert, D., Riek, R., 2005. 3D structure of Alzheimer's amyloid-β(1–42) fibrils. PNAS 102, 17342–17347.

MacPhee, C.E., Woolfson, D.N., 2004. Engineered and designed peptide-based fibrous biomaterials. Curr. Opin. Solid State Mater. Sci. 8, 141–149.

Makin, O.S., Serpell, L.C., 2005. Structures for amyloid fibrils. FEBS J. 272, 5950–5961.

Makin, O.S., Atkins, E., Sikorski, P., Johansson, J., Serpell, L.C., 2005. Molecular basis for amyloid fibril formation and stability. PNAS 102, 315–320.

Morimoto, A., Irie, K., Murakami, K., Masuda, Y., Ohigashi, H., Nagao, M., Fukuda, H., Shimizu, T., Shirasawa, T., 2004. Analysis of the secondary structure of beta-amyloid (Abeta42) fibrils by systematic proline replacement. J. Biol. Chem. 279, 52781–52788.

Morris, G.A., Freeman, R., 1979. Enhancement of nuclear magnetic-resonance signals by polarization transfer. J. Am. Chem. Soc. 101, 760–762.

Morris, K., Serpell, L., 2010. From natural to designer self-assembling biopolymers, the structural characterisation of fibrous proteins & peptides using fibre diffraction. Chem. Soc. Rev. 39, 3445–3453.

Nelson, R., Sawaya, M.R., Balbirnie, M., Madsen, A.Ø., Riekel, C., Grothe, R., Eisenberg, D., 2005. Structure of the cross-β spine of amyloid-like fibrils. Nature 435, 773–778.

Pagel, K., Seri, T., von Berlepsch, H., Griebel, J., Kirmse, R., Bottcher, C., Koksch, B., 2008b. How metal ions affect amyloid formation: Cu2+- and Zn2+-sensitive peptides. Chembiochem 9, 531–536.

Pagel, K., Koksch, B., 2008. Following polypeptide folding and assembly with conformational switches. Curr. Opin. Chem. Biol. 12, 730–739.

Pagel, K., Vagt, T., Kohajda, T., Koksch, B., 2005. From [small alpha]-helix to [small beta]-sheet - a reversible metal ion induced peptide secondary structure switch. Org. Biomol. Chem. 3, 2500–2502.

Pagel, K., Wagner, S.C., Samedov, K., von Berlepsch, H., Böttcher, C., Koksch, B., 2006.

Random coils, β-sheet ribbons, and α-helical fibers: one peptide adopting three different secondary structures at will. J. Am. Chem. Soc. 128, 2196–2197.
Pagel, K., Wagner, S.C., Rezaei Araghi, R., von Berlepsch, H., Böttcher, C., Koksch, B., 2008a. Intramolecular charge interactions as a tool to control the coiled-coil-to-amyloid transformation. Chem. Eur. J. 14, 11442–11451.
Paris, O., Li, C., Siegel, S., Weseloh, G., Emmerling, F., Riesemeier, H., Erkod, A., Fratzl, P., 2007. A new experimental station for simultaneous X-ray microbeam scanning for small- and wide-angle scattering and fluorescence at BESSY II. J. Appl. Crystallogr. 40, S466–S470.
Pauli, J., Baldus, M., van Rossum, B., de Groot, H., Oschkinat, H., 2001. Backbone and side-chain 13C and 15N signal assignments of the alpha-spectrin SH3 domain by magic angle spinning solid-state NMR at 17.6 Tesla. Chembiochem 2272–2281.
Petkova, A.T., Ishii, Y., Balbach, J.J., Antzutkin, O.N., Leapman, R.D., Delaglio, F., Tycko, R., 2002. A structural model for Alzheimer's β-amyloid fibrils based on experimental constraints from solid state NMR. Proc. Natl. Acad. Sci. 99, 16742–16747.
Petkova, A.T., Buntkowsky, G., Dyda, F., Leapman, R.D., Yau, W.M., Tycko, R., 2004. Solid state NMR reveals a pH-dependent antiparallel beta-sheet registry in fibrils formed by a beta-amyloid peptide. J. Mol. Biol. 335, 247–260.
Psonka-Antonczyk, K.M., Hammarstrom, P., Johansson, L.B., Lindgren, M., Stokke, B.T., Nilsson, K.P., Nystrom, S., 2016. Nanoscale structure and spectroscopic probing of Abeta1-40 fibril bundle formation. Front. Chem. 4, 44.
Qiang, W., Yau, W.M., Lu, J.X., Collinge, J., Tycko, R., 2017. Structural variation in amyloid-beta fibrils from Alzheimer's disease clinical subtypes. Nature 541, 217–221.
Rieping, W., Habeck, M., Bardiaux, B., Bernard, A., Malliavin, T.E., Nilges, M., 2007. ARIA2: automated NOE assignment and data integration in NMR structure calculation. Bioinformatics (Oxford, England) 23, 381–382.
Rousseau, F., Schymkowitz, J., Serrano, L., 2006. Protein aggregation and amyloidosis: confusion of the kinds? Curr. Opin. Struct. Biol. 16, 118–126.
Selkoe, D.J., 2003. Folding proteins in fatal ways. Nature 426, 900–904.
Seo, J., Hoffmann, W., Warnke, S., Huang, X., Gewinner, S., Schöllkopf, W., Bowers, M.T., von Helden, G., Pagel, K., 2016. An infrared spectroscopy approach to follow β-sheet formation in peptide amyloid assemblies. Nat. Chem. 9, 39.
Shen, Y., Delaglio, F., Cornilescu, G., Bax, A., 2009. TALOS+: a hybrid method for predicting protein backbone torsion angles from NMR chemical shifts. J. Biomol. NMR 44, 213–223.
Squires, A.M., Devlin, G.L., Gras, S.L., Tickler, A.K., MacPhee, C.E., Dobson, C.M., 2006. X-ray scattering study of the effect of hydration on the cross-beta structure of amyloid fibrils. J. Am. Chem. Soc. 128, 11738–11739.
Stefani, M., Dobson, C.M., 2003. Protein aggregation and aggregate toxicity: new insights into protein folding, misfolding diseases and biological evolution. J. Mol. Med. (Berlin, Germany) 81, 678–699.
Stevens, T.J., Fogh, R.H., Boucher, W., Higman, V.A., Eisenmenger, F., Bardiaux, B., van Rossum, B.J., Oschkinat, H., Laue, E.D., 2011. A software framework for analysing solid-state MAS NMR data. J. Biomol. NMR 51, 437–447.
Straus, S.K., Bremi, T., Ernst, R.R., 1998. Experiments and strategies for the assignment of fully13C/15N-labelled polypeptides by solid state NMR. J. Biomol. NMR 12, 39–50.
Stubbs, G., 1999. Developments in fiber diffraction. Curr. Opin. Struct. Biol. 9, 615–619.
Sunde, M., Serpell, L.C., Bartlam, M., Fraser, P.E., Pepys, M.B., Blake, C.C., 1997. Common core structure of amyloid fibrils by synchrotron X-ray diffraction. J. Mol. Biol. 273, 729–739.
Szeverenyi, N.M., Sullivan, M.J., Maciel, G.E., 1982. Observation of spin exchange by two-dimensional fourier transform ^{13}C cross polarization-magic-angle spinning. J. Magn. Reson. 47, 462–475.
Tycko, R., 2011. Solid-state NMR studies of amyloid fibril structure. Annu. Rev. Phys. Chem. 62, 279–299.
Vranken, W.F., Boucher, W., Stevens, T.J., Fogh, R.H., Pajon, A., Llinas, M., Ulrich, E.L., Markley, J.L., Ionides, J., Laue, E.D., 2005. The CCPN data model for NMR spectroscopy: development of a software pipeline. Proteins Struct. Funct. Genet. 59, 687–696.
Wälti, M.A., Ravotti, F., Arai, H., Glabe, C.G., Wall, J.S., Böckmann, A., Güntert, P., Meier, B.H., Riek, R., 2016. Atomic-resolution structure of a disease-relevant Aβ(1–42) amyloid fibril. Proc. Natl. Acad. Sci. 113, E4976–E4984. http://dx.doi.org/10.1073/pnas.1600749113.
Williams, A.D., Portelius, E., Kheterpal, I., Guo, J.T., Cook, K.D., Xu, Y., Wetzel, R., 2004. Mapping abeta amyloid fibril secondary structure using scanning proline mutagenesis. J. Mol. Biol. 335, 833–842.
Williams, A.D., Shivaprasad, S., Wetzel, R., 2006. Alanine scanning mutagenesis of Abeta (1–40) amyloid fibril stability. J. Mol. Biol. 357, 1283–1294.
Zhang, C., Mortuza, S.M., He, B., Wang, Y., Zhang, Y., 2017. Template-based and free modeling of I-TASSER and QUARK pipelines using predicted contact maps in CASP12. Proteins: Struct. Funct. Bioinf. 1–16.